Two-valence band electron and heat transport in monocrystalline PbTe-CdTe solid solutions with Cd content up to 10 atomic percent

M. Szot,[1,*] P. Pfeffer,[1] K. Dybko,[1,2] A. Szczerbakow,[1] L. Kowalczyk,[1] P. Dziawa,[1] R. Minikayev,[1] T. Zajarniuk,[1] K. Piotrowski,[1] M. U. Gutowska,[1] A. Szewczyk,[1] T. Story,[1,2] and W. Zawadzki[1]

[1]*Institute of Physics, Polish Academy of Sciences, Aleja Lotnikow 32/46, PL-02668 Warsaw, Poland*

[2]*International Research Centre MagTop, Institute of Physics, Polish Academy of Sciences, Aleja Lotnikow 32/46, PL-02668 Warsaw, Poland*

(Received 15 November 2019; revised manuscript received 13 March 2020; accepted 19 March 2020; published 29 April 2020)

High-quality *p*-type PbTe-CdTe monocrystalline alloys containing up to 10 at.% of Cd have been obtained by self-selecting vapor transport method. Mid-infrared photoluminescence experiments have been performed in order to follow the variation of the fundamental energy gap as a function of Cd content. The Hall mobility, thermoelectric power, thermal conductivity, and thermoelectric figure-of-merit parameter ZT were investigated experimentally and theoretically with special attention paid to the two-valence band structure of the material. It is shown that the heavy-hole band near the Σ point of the Brillouin zone plays an important role and is responsible for the $Pb_{1-x}Cd_xTe$ hole transport at higher Cd content. Our data and their description can serve as monocrystalline reference for $Pb_{1-x}Cd_xTe$ crystals with x up to 0.1. It is shown that monocrystalline $Pb_{1-x}Cd_xTe$ samples with relatively low Cd content of about 1 at.% and hole concentration of the order of 10^{20} cm^{-3} may exhibit $ZT \approx 1.4$ at 600 K.

DOI: 10.1103/PhysRevMaterials.4.044605

I. INTRODUCTION

Lead chalcogenides are IV-VI narrow-gap semiconductors known for thermoelectric and mid-infrared applications [1–3]. An incorporation of tin into their cation sublattice leads to a decrease of the fundamental energy gap at the L points of the Brillouin zone which, in the case of $Pb_{1-x}Sn_xTe$ and $Pb_{1-x}Sn_xSe$ alloys, results in the band inversion giving rise to the formation of topological crystalline insulators [4,5]. On the other hand, an addition of Mn, Eu, Sr, or Mg ions to lead chalcogenides leads to an increase of the fundamental gap and, consequently, to an increase of the effective light-hole and electron masses [6–12]. This enhances the thermoelectric power, lowers carrier's mobility, and changes other thermodynamic characteristics. Similar effect is expected for alloying PbTe with CdTe. In particular, it was suggested that the substitution of Pb ions by Cd ones may introduce a resonant level in the band structure of PbTe, resulting in an enhancement of the Seebeck coefficient through a distortion of the density of states near the bottom of the conduction band [13,14]. That corresponds to the case of *p*-type $Pb_{1-x}Tl_xTe$, where the resonant level is introduced in the valence band [15]. However, due to different crystal structures of both materials, rock salt for PbTe and zinc blende for CdTe, these materials exhibit extremely low mutual solubility when grown from the melt [16–19]. Their alloying leads usually to a formation of highly symmetric (with rhombo-cubo-octahedron shape) zinc-blende precipitations of CdTe in the rock-salt PbTe [20,21], for sufficiently high CdTe content [22–24]. The almost perfect lattice parameter matching between PbTe (6.46 Å) and CdTe (6.48 Å) results in atomically sharp PbTe/CdTe interfaces, thus permitting a new approach to the crystal-coherent two-phase thermoelectric system. For this reason, none or very weak effects of alloying PbTe with CdTe on thermoelectric power were reported for $Pb_{1-x}Cd_xTe$ ($x \leqslant 0.03$) polycrystalline samples obtained by rapid quenching or hot pressing methods. The latter growth technique is prone to the formation of CdTe nanoinclusions and microinclusions in the polycrystalline matrix, which contribute to the reduction of thermal conductivity and in consequence to the increase of thermoelectric figure-of-merit parameter up to $ZT \approx 1.7$ for such two-phase material [13,14,25].

In this paper we present the experimental and theoretical study of the effect of Cd ions on optical and thermoelectric properties of $Pb_{1-x}Cd_xTe$ monocrystalline solid solutions with x up to 0.1 obtained by self-selecting vapor growth (SSVG) method [26–28]. Special attention is paid to two-valence band character of the hole transport. It is worth to note that, while polycrystals of $Pb_{1-x}Cd_xTe$ had been available for investigations [29], the single crystals with the Cd content $x \geqslant 0.02$ were not examined. In this sense, our data and conclusions can serve as a monocrystalline reference standard for the material. This is even more important in view of the fact that $Pb_{1-x}Cd_xTe$ has been for a long time a material of controversy, beginning with the relative positions of the light- and heavy-hole bands, the value of hole mobility, thermoelectric power, and, finally, with regard to its thermoelectric figure of merit. Precise analysis of its properties has been obscured by the two valence bands contributing to the transport properties. For this reason, PbTe and $Pb_{1-x}Cd_xTe$ are not classical narrow-gap semiconductors, although they have been considered as such.

*szot@ifpan.edu.pl

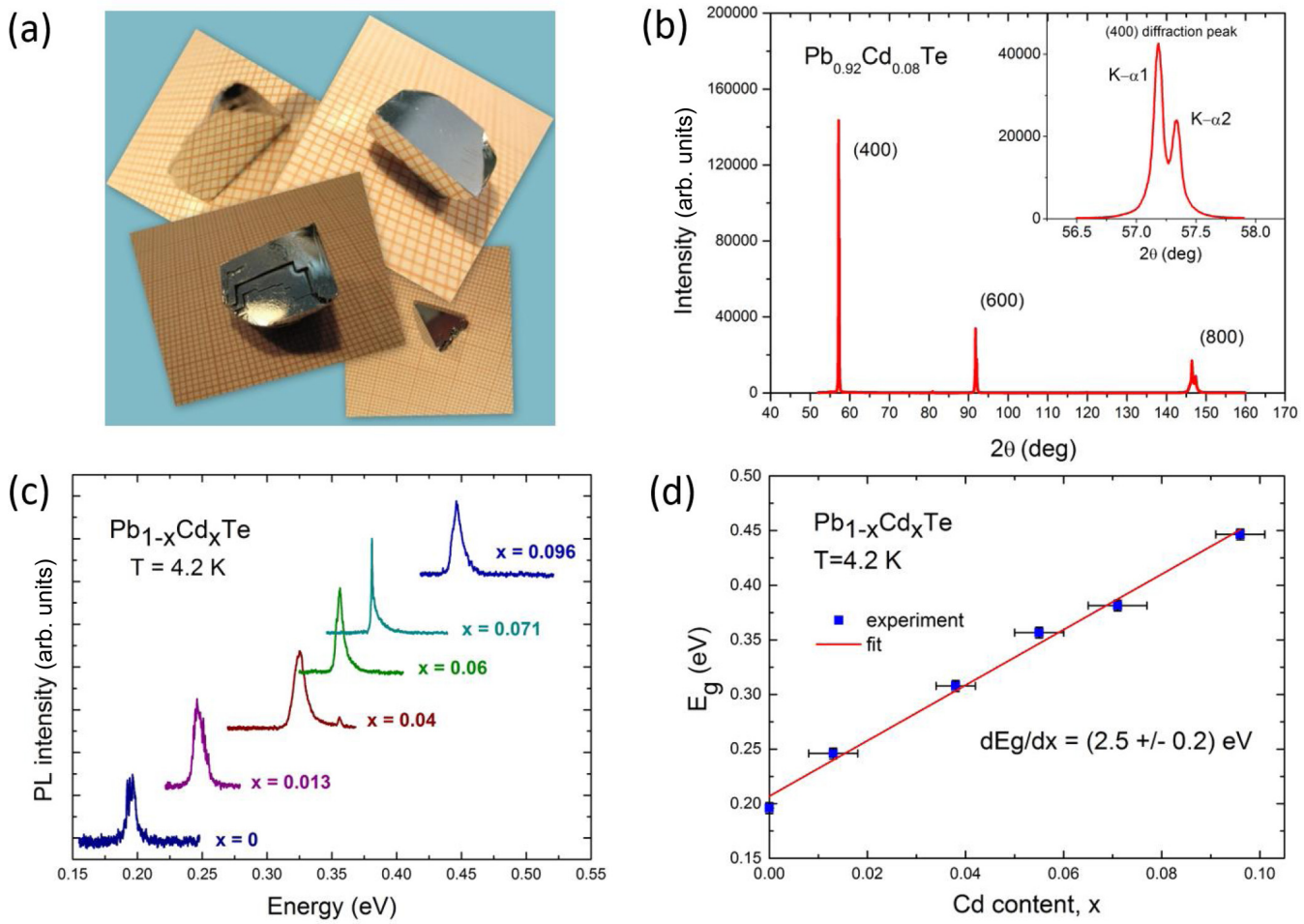

FIG. 1. (a) $Pb_{1-x}Cd_xTe$ monocrystals obtained by the SSVG method (crystals are located on the millimeter grid paper). (b) X-ray diffraction spectra of $Pb_{0.92}Cd_{0.08}Te$ monocrystals. (c) Photoluminescence spectra of $Pb_{1-x}Cd_xTe$ samples at 4.2 K for different Cd content x. (d) The dependence of the energy gap $E_g = E_{L_6^-} - E_{L_6^+}$ of $Pb_{1-x}Cd_xTe$ at 4.2 K on Cd content x.

II. SAMPLE PREPARATION AND EXPERIMENT

The SSVG method was chosen for preparation of monocrystalline $Pb_{1-x}Cd_xTe$ as exceptionally suitable for growth of IV-VI compounds. It was confirmed in the case of $Pb_{1-x}Sn_xTe$ and $Pb_{1-x}Sn_xSe$ crystals [4,30,31]. The samples were grown from polycrystalline PbTe and CdTe synthesized with excessive Te and Cd, respectively. The growth temperatures determined by the PbTe-CdTe phase diagram were about 850–870 °C, i.e., below the melting point of PbTe [16,17]. During the process, the material placed inside the quartz ampoule evaporates from the hotter part of the polycrystalline source and then condenses in its cooler region. The transport of the material inside the ampoule was driven by a small (few degrees) temperature gradient controlled by multizone electric oven with special temperature profile, in which the growth was performed [27]. The obtained monocrystalline samples with the Cd content up to $x = 0.102$ are shown in Fig. 1(a). After the growth process, the ampoule was removed from the oven to the laboratory environment. That ensures a very fast cooling of the crystal to the temperature of about 400 °C. As it results from the PbTe-CdTe phase diagram, below this temperature the crystal structure of $Pb_{1-x}Cd_xTe$ solid solution is practically frozen [32]. Such a post-growth cooling method is sufficiently fast to prevent a phase separation in the case of investigated mixed crystals. Monocrystals produced by SSVG are known to exhibit exceptional homogeneity. Uniform distribution of cadmium ions in the whole volume of individual $Pb_{1-x}Cd_xTe$ crystals was confirmed by determination of Cd content in various parts of the "as-grown" crystal using the scanning electron microscopy (SEM) with energy dispersive x-ray fluorescence method (see tables in Fig. 2 and Fig. 3). The experimental uncertainty of Cd content in the investigated samples does not exceed 0.6 at.%.

Crystal quality of obtained samples was verified by x-ray diffraction (XRD) measurements carried out with the use of X'Pert Pro Alpha 1 MPD (Panalytical) diffractometer. Monocrystalline as well as powdered samples were examined. XRD spectra shown in Fig. 1(b), obtained for monocrystals, were used to establish the lattice parameter and consequently da_0/dx ratio [26]. Powder x-ray spectra (see Fig. 4) do not show a presence of a second phase in investigated $Pb_{1-x}Cd_xTe$ samples for all x studied. The $Pb_{1-x}Cd_xTe$ samples were examined optically by photoluminescence measurements performed in wide range of temperatures, $T =$ 4–120 K, using 1064 nm line of pulsed YAG:Nd laser for

$Pb_{0.91}Cd_{0.09}Te$

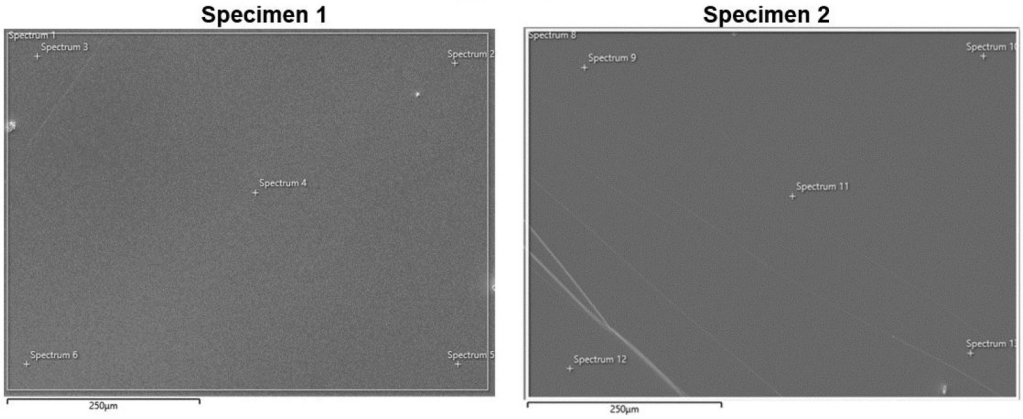

Table 1 Area measurement

Cd cont. x	x dev.	anions	dev.
0.094	0.011	0.491	0.007

Point measurements

	Cd cont. x	x dev.	anions	dev.
pt. 1	0.082	0.011	0.492	0.008
pt. 2	0.083	0.011	0.493	0.008
pt. 3	0.086	0.011	0.495	0.008
pt. 4	0.094	0.012	0.487	0.008
pt. 5	0.105	0.011	0.480	0.008
<pts>	0.090	0.008	0.490	0.005

Table 2 Area measurement

Cd cont. x	x dev.	anions	dev.
0.091	0.005	0.491	0.003

Point measurements

	Cd cont. x	x dev.	anions	dev.
pt. 1	0.091	0.005	0.488	0.003
pt. 2	0.090	0.005	0.489	0.003
pt. 3	0.094	0.005	0.489	0.004
pt. 4	0.098	0.005	0.483	0.004
pt. 5	0.094	0.005	0.485	0.004
<pts>	0.093	0.002	0.487	0.002

FIG. 2. SEM micrograph of two specimens cleaved from $Pb_{0.91}Cd_{0.09}Te$ monocrytal with a volume of about 1 ccm. In the tables, the Cd content x data obtained by EDX measurement from the area of (700 × 700) μm and from few points within this zone are collected.

excitation [see Figs. 1(c) and 1(d), 5 and 6 in the text). Samples were cleaved from the host material shortly before the measurements to minimize the influence of oxidation processes on experimental results [33]. The carrier concentration and mobility in $Pb_{1-x}Cd_xTe$ samples were determined by measurements of the Hall effect employing the standard Hall bar geometry with six contacts. To determine the Seebeck coefficient α (thermopower), the samples were mounted between two independent heaters. Two thermocouples were used to measure the temperature gradient along the samples and to determine the Seebeck voltage. The value of thermopower for a given sample was determined as the average of measurements performed for different temperature gradients applied in both directions. The room-temperature thermal conductivity κ was measured for several $Pb_{1-x}Cd_xTe$ samples with different Cd content as well as for pure PbTe. The measurements were performed on separately cleaved samples with dimensions 5 × 5 × 5 mm, suitable for measurements with Physical Property Measurment System (PPMS). Finally, the figure-of-merit parameter ZT was also determined directly by the Harman method [2,34,35].

III. THEORY

It is known that that the hole transport in PbTe and $Pb_{1-x}Cd_xTe$ is governed by two valence bands: of the light holes (LH) with their minima at the L points and of the heavy-holes (HH) near the Σ points of the Brillouin zone, as is shown in Fig. 7(a). The relative energy positions of these bands are a subject of a long dispute (Jaworski *et al.* [36] and the Appendix) and our work also contributes to the light and heavy holes bands' location. In Fig. 7(b) we show the band edges of the two valence bands and one conduction band of $Pb_{1-x}Cd_xTe$, as determined in our analysis. The light-hole (LH) valence bands in PbTe and $Pb_{1-x}Cd_xTe$ are both nonspherical and nonparabolic. The nonsphericity is due to the location of bands' minima at the L points, while the nonparabolicity is caused by the small energy gap E_g and the resulting strong $\mathbf{k}\cdot\mathbf{p}$ interaction with the conduction bands. Because the overall symmetry of the ellipsoid ensemble is cubic, as required by rock-salt crystal symmetry, for the analysis of the scattering mechanism we approximate it by one spherical energy band with the corresponding nonparabolicity. In the $\mathbf{k}\cdot\mathbf{p}$ two-band model the nonparabolic dispersion

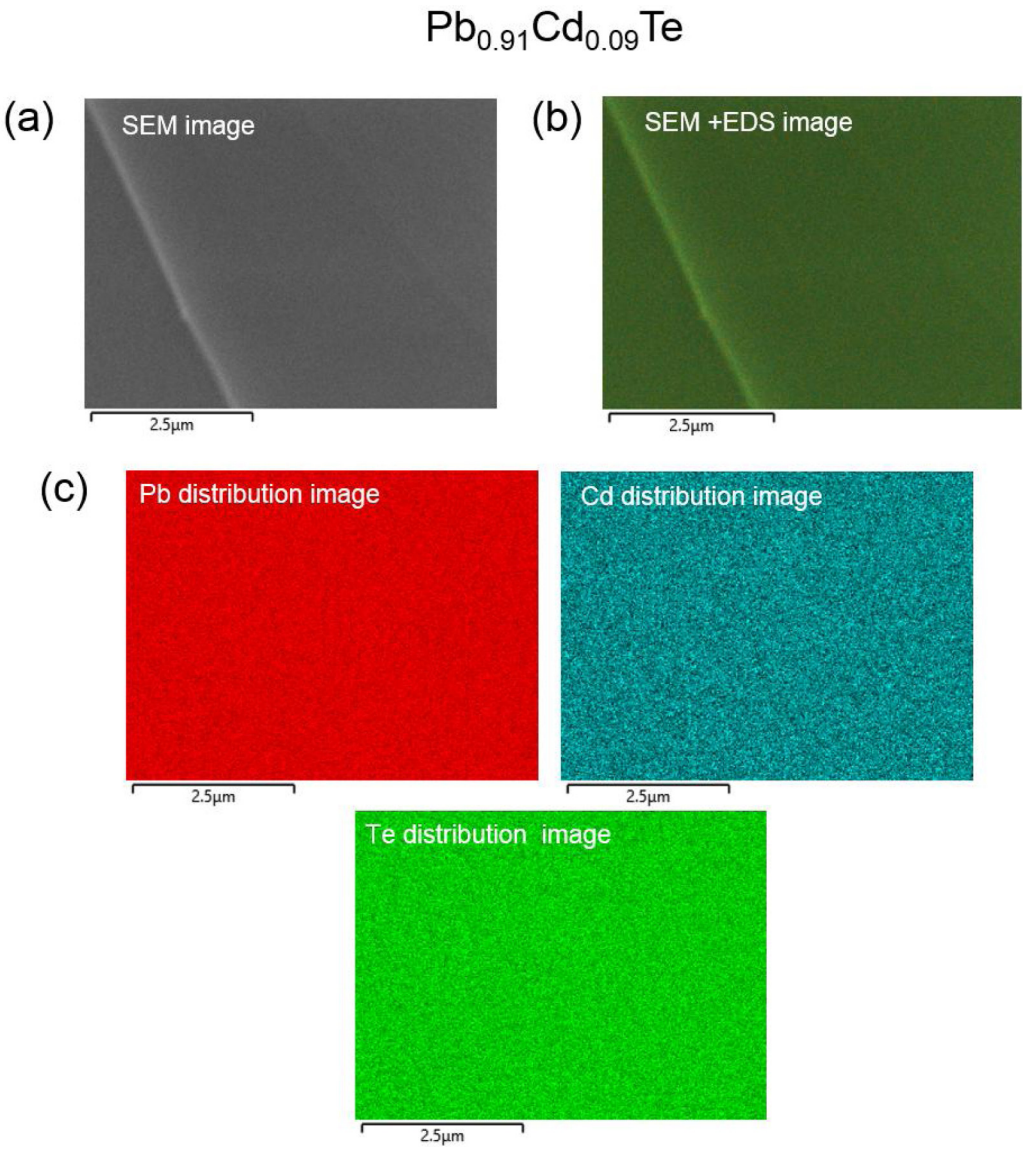

FIG. 3. (a) SEM and (b) SEM+EDS images of $Pb_{0.91}Cd_{0.09}Te$ sample, (c) distribution of Pb, Te, Cd elements collected within (5×5) μm area of the sample.

is [37]

$$\mathcal{E} = -\frac{E_g}{2} + \left[\left(\frac{E_g}{2}\right)^2 + \frac{E_g \hbar^2 k^2}{2m_0^*}\right]^{1/2}, \tag{1}$$

where the zero of energy $\mathcal{E}$ is chosen at the valence band edge and $m_0^* = 0.068m_0$ is the average effective mass at the edge.

The anisotropy of the effective mass of light holes in PbTe is characterized by $m_\parallel^*/m_\perp^* = 10.8$ at $T = 4$ K and at $T = 300$ K. In the case of the transport phenomena, for description of carriers' scattering and carriers' mobility the density of states effective mass is $m_d^* = (m_\parallel^* m_\perp^{*\,2})^{1/3} = 0.086m_0$ and the conductivity mass is $m_c^* = 3/(m_\parallel^{*-1} + 2m_\perp^{*-1}) = 0.056m_0$ at $T = 300$ K. In PbTe m_d^* and m_c^* effective masses differ only slightly, so in our calculations we use spherical effective mass of light holes m_0^* at the edge of valence band, as averaged between m_d^* and m_c^*.

The resulting energy-dependent effective mass relating velocity to pseudomomentum k is

$$m^*(\mathcal{E}) = m_0^*\left(1 + \frac{2\mathcal{E}}{E_g}\right), \tag{2}$$

where

$$m_0^* = \frac{3E_g\hbar^2}{4P^2}, \tag{3}$$

where P is the interband matrix element of momentum (see Zawadzki [38]). We described the composition and temperature dependence of $E_g(x, T)$ for $Pb_{1-x}Cd_xTe$ using our low-temperature photoluminescence data and empirical Varshni-type formula [39] (see Fig. 6)

$$E_g(x, T)(\text{meV}) = 188 + 2533x + \frac{0.5T^2}{T + 55}. \tag{4}$$

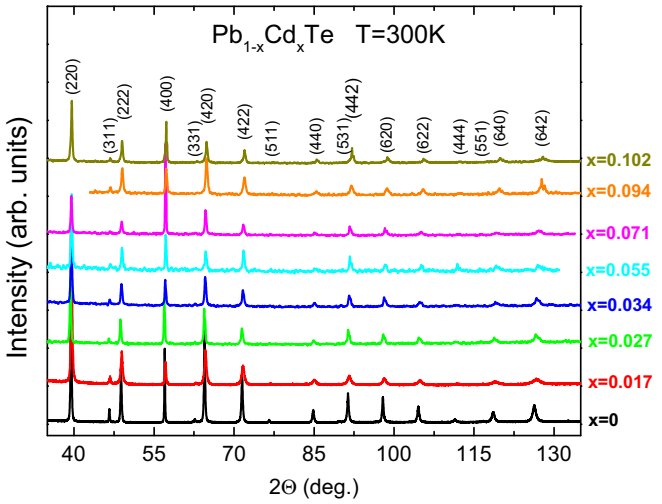

FIG. 4. X-ray diffraction spectra of powdered $Pb_{1-x}Cd_xTe$ samples with Cd content $0 \leqslant x \leqslant 0.102$.

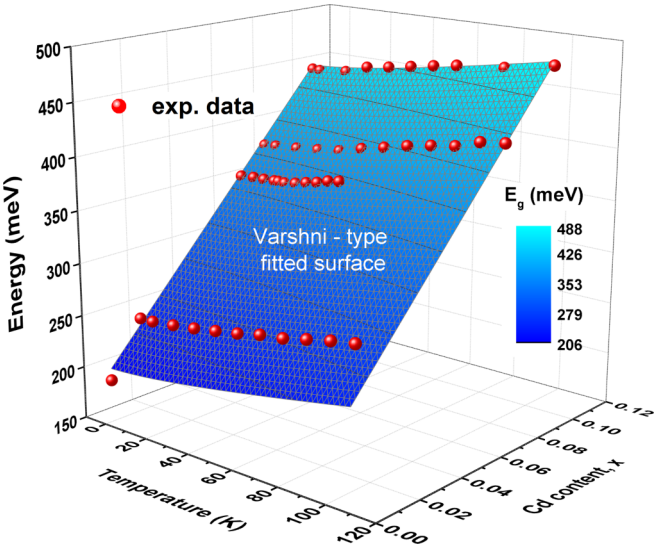

FIG. 6. Dependence of E_g for $Pb_{1-x}Cd_xTe$ samples on temperature and Cd content x described using Varshni-type formula [see Eq. (4)].

The room-temperature L-point energy gap for pure PbTe resulting from this formula is overestimated only slightly (less than 2%) comparing to the experimental value 310 meV [40]. It indicates that Eq. (4) describes quite well $E_{g,L}$ for $Pb_{1-x}Cd_xTe$ up to 300 K. However, at higher temperatures the difference between experimental values of E_g for PbTe and those following from Eq. (4) increases reaching over 20% at 600 K [41]. Thus, for consistency, in our calculations for all temperatures studied we decided to use the values of E_g for $Pb_{1-x}Cd_xTe$ resulting from the modification of experimental $E_{g,L}$ for PbTe by $dE_g/dx = 2.5$ eV factor obtained from our data [see Fig. 1(d) and Eq. (4)]. The corresponding edge mass is

$$\frac{m_0^*}{m_0} = \frac{E_g(\text{eV})}{4.08 + 1.6 \times 10^{-3} T}. \tag{5}$$

For nonparabolic bands the transport quantities are described in general by the integrals [38]

$$\langle A \rangle = \int_0^\infty \left(-\frac{\partial f_0(\mathcal{E})}{\partial \mathcal{E}} \right) A(\mathcal{E}) k^3 d\mathcal{E}, \tag{6}$$

where f_0 is the Fermi-Dirac distribution function. In this notation the carrier density is $N = \int_0^\infty f_0(\mathcal{E})\rho(\mathcal{E})d\mathcal{E} = l/3\pi^2\langle 1\rangle$, where $l = l_{lh} = 4$ for light holes. Carrier mobility is given by $\mu(\mathcal{E}) = q\tau(\mathcal{E})/m^*(\mathcal{E})$, where $\tau(\mathcal{E})$ is the total relaxation time. Various scattering mechanisms are described by separate τ_i and the total relaxation time is $\tau^{-1} = \sum_i \tau_i^{-1}$.

Carrier density is calculated using the relation $N = A_r/(qR_H) = A_r N_H$, where R_H is the measured Hall coefficient, N_H is the Hall carrier density, and A_r is the Hall scattering factor. Taking into account the mass anisotropy

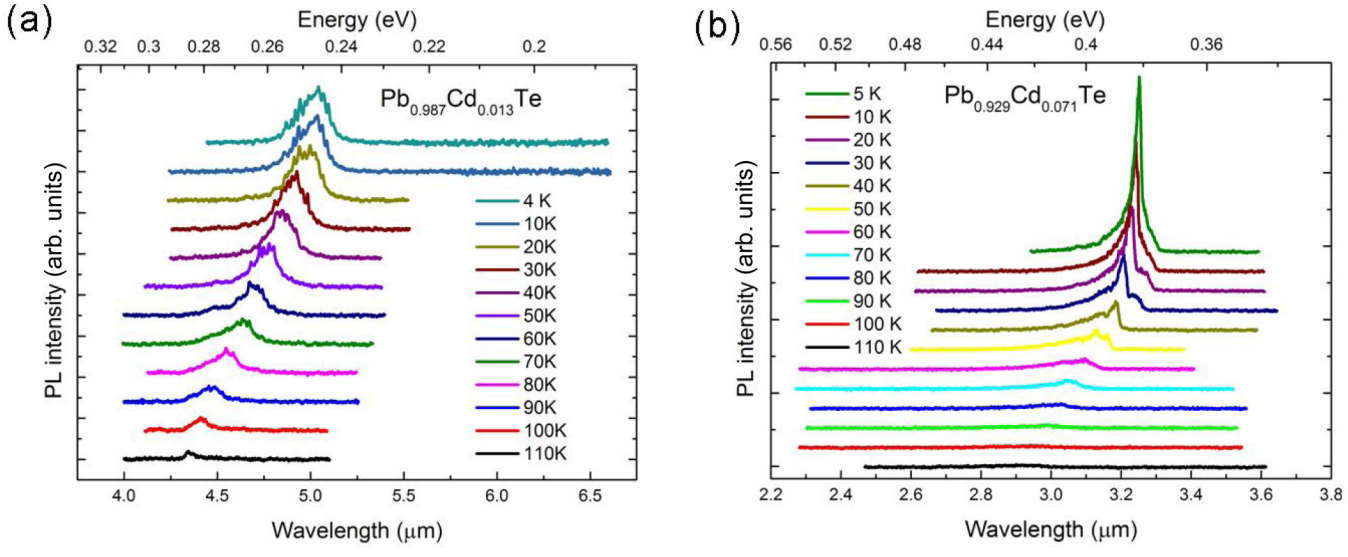

FIG. 5. Photoluminesce of $Pb_{1-x}Cd_xTe$ monocrystals with (a) $x = 0.013$ and (b) $x = 0.071$ measured at temperatures from 4 to 110 K.

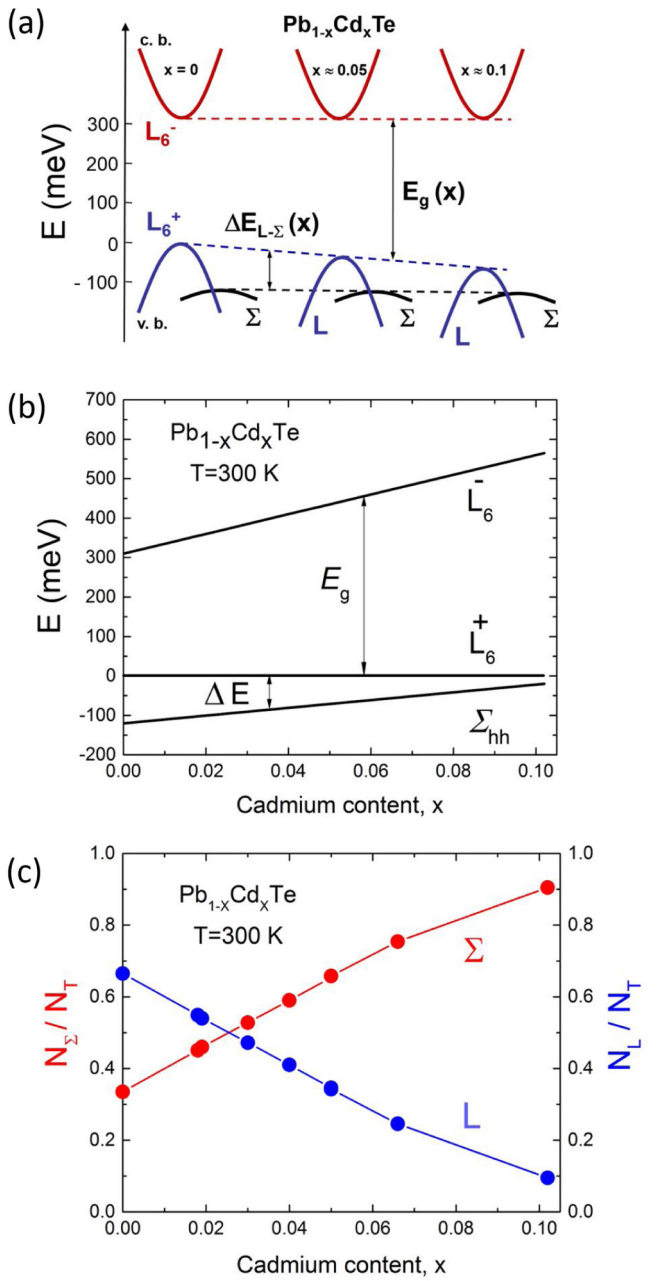

FIG. 7. (a) $Pb_{1-x}Cd_xTe$ band structure evolution on Cd content at 300 K. (b) Relative energies of two-valence band edges: Σ_{hh} and L_6^+, and the conduction band edge L_6^- in $Pb_{1-x}Cd_xTe$ versus Cd content x, as established and adjusted in the present analysis for $T = 300$ K. The light-hole effective mass is proportional to E_g. (c) Ratio of the heavy-hole density N_Σ (left scale) and light-hole density N_L (right scale) to the total density N_T in both valence bands versus Cd content x, corresponding to the energies shown in (b).

$K = m_\parallel^*/m_\perp^*$, there is

$$A_r = \frac{3K(K+2)}{(2K+1)^2}\frac{\overline{\mu^2}}{(\overline{\mu})^2}, \tag{7}$$

where the average mobility $\overline{\mu} = \langle\mu\rangle/\langle 1\rangle$. For PbTe $\frac{3K(K+2)}{(2K+1)^2} = 0.812$ for light holes. The electric conductivity in the absence of magnetic field is

$$\sigma = qN\overline{\mu} = qN_H\mu_H, \tag{8}$$

where $\overline{\mu} = \mu_H/A_r$ and μ_H is the Hall mobility.

The Seebeck coefficient is given by [38]

$$\alpha = \frac{k_B}{q}\left(\frac{\langle z\mu\rangle}{\langle\mu\rangle} - \eta\right), \tag{9}$$

where $z = E/k_BT$ and $\eta = E_F/k_BT$ in which E_F is the Fermi energy and $\langle\ldots\rangle$ denotes the integral over the band [see Eq. (5)].

The thermal conductivity consists of the lattice and carrier contributions: $\kappa = \kappa_L + \kappa_c$, where κ_L at $T = 300$ K is [42,43]

$$\kappa_L = \left[\frac{1}{\kappa_{Lp}} + \frac{\Omega_0}{4\pi\vartheta_s^3}x(1-x)\Gamma\right]^{-1}, \tag{10}$$

where κ_{Lp} is the thermal conductivity of pure PbTe, Ω_0 is the volume of the unit cell, ϑ_s is the velocity of sound, Γ is the parameter dependent on the mass of unit cell. The carrier part of thermal conductivity is [38]

$$\kappa_c = T\left(\frac{k_B}{q}\right)^2\sigma\left(\frac{\langle z^2\mu\rangle}{\langle\mu\rangle} - \frac{\langle z\mu\rangle^2}{\langle\mu\rangle^2}\right). \tag{11}$$

Finally, the thermoelectric figure-of-merit parameter is defined as

$$ZT = \frac{\alpha^2\sigma}{\kappa}T. \tag{12}$$

The band of heavy holes is far away from other bands at the same k value. In consequence, it is described by the standard parabolic approximation $E = \hbar^2k^2/2m_{hh}^*$, where the adjusted mass is $m_{hh}^* = 0.6m_0$ (see the discussion below). The expressions for the parabolic band given above and below are formally obtained from the description of nonparabolic ones by putting $E_g \to \infty$ (limit of noninteracting valence band and conduction band). The number of HH ellipsoids is $l = l_{hh} = 12$. We further assume that the HH mass does not depend on the temperature and the Cd content x and take the anisotropy factor in Eq. (7) equal to unity. This is justified by a large direct gap at Σ points. In the two-band calculations the Fermi level is imposed to be the same for both bands.

For the two-band transport formulas we used the standard expressions [44]

$$\mu = \frac{\overline{\mu_L}N_L + \overline{\mu_\Sigma}N_\Sigma}{N_T}, \tag{13}$$

where $\overline{\mu_L}, \overline{\mu_\Sigma}, N_L, N_\Sigma$ are mobilities and concentrations of light and heavy holes, respectively, and $N_T = N_L + N_\Sigma$.

The Seebeck coefficent is [44]

$$\alpha = \frac{\alpha_L\overline{\mu_L}N_L + \alpha_\Sigma\overline{\mu_\Sigma}N_\Sigma}{\overline{\mu_L}N_L + \overline{\mu_\Sigma}N_\Sigma}, \tag{14}$$

where α_L and α_Σ are the corresponding quantities for the light and heavy holes, respectively.

In order to calculate the transport quantities, one needs to know and describe dominant scattering mechanisms. The relaxation times are determined by the scattering probabilities for which one needs to know the hole wave functions. Since the light-hole band L_6^+ and the conduction band L_6^- are

energetically close, their wave functions are mixtures of both bands. The L_6^+ spin-up and spin-down bands are [45]

$$\Psi_v^{\uparrow} = \left[\sqrt{(1-L)}iR + \frac{L}{k}(k_z cZ - k_- dX_-)\right]\uparrow - \frac{L}{k}(k_z cZ - k_z dX_+)\downarrow,$$
$$\Psi_v^{\downarrow} = \left[\sqrt{(1-L)}iR + \frac{L}{k}(k_z cZ - k_+ dX_+)\right]\downarrow + \frac{L}{k}(k_+ cZ + k_z dX_-)\uparrow, \quad (15)$$

where $X_\pm = (X \pm iY)/\sqrt{2}$, $L = \mathcal{E}/(2\mathcal{E} + E_g)$, $k_\pm = k_x \pm ik_y$, R is the periodic amplitude of Luttinger-Kohn functions at the L point of the Brillouin zone, and the normalization coefficients c and d fulfill the condition $c^2 + d^2 = 1$. The effective spin-up ($\uparrow$) and spin-down ($\downarrow$) functions are indicated in the overscripts.

First, we consider the polar scattering caused by the polar interaction between longitudinal optic phonons and holes. It is described by the following formula taking into account both the screening by the hole gas as well as the phonon frequency dependence on the hole density [45]:

$$(\tau^{po})^{-1}(k) = \frac{kTe^2}{\hbar^2}\left(\frac{1}{\varepsilon_\infty} - \frac{1}{\varepsilon_0}\right)\frac{F_{po}(2\mathcal{E} + E_g)}{\sqrt{\mathcal{E} + E_g}}\sqrt{\frac{2m_0^*}{E_g\mathcal{E}}} = \frac{2kTe^2}{\hbar}\left(\frac{1}{\varepsilon_\infty} - \frac{1}{\varepsilon_0}\right)\frac{dk}{d\mathcal{E}}F_{po}, \quad (16)$$

where

$$F_{po} = \left[1 - \frac{ln(1+\rho_\infty)}{\rho_\infty}\right] - 2H\left[1 - \frac{2}{\rho_\infty} + 2\frac{ln(1+\rho_\infty)}{{\rho_\infty}^2}\right], \quad (17)$$

$H = L(1-L)$, and $\rho_\infty = 4k^2{\lambda_\infty}^2$, where

$$\frac{1}{{\lambda_\infty}^2} = \frac{2le^2}{\pi\varepsilon_\infty}\left\langle\frac{(E_g + 2\mathcal{E})}{(E_g + \mathcal{E})\mathcal{E}}\right\rangle \quad (18)$$

and λ_∞ is the screening length for the high-frequency dielectric constant. We use for polar optical scattering the relaxation time approximation because $\hbar\omega_{op}/k_BT \simeq 1/2$. For lower temperatures (nonelastic scattering), one needs variational methods [46].

The other three important scattering mechanisms are caused by the deformation potentials with acoustic and optical phonons and by alloy disorder. For acoustic phonons the relaxation time is [45]

$$(\tau_{ac})^{-1}(k) = C_{ac}\left(E_{ac}^v\right)^2 F_{ac}, \quad (19)$$

$$C_{ac} = \frac{k_BT}{\pi\hbar c_1}\frac{\partial k}{\partial\mathcal{E}}k^2, \quad (20)$$

where the acoustic deformation potentials are $E_{ac}^v = E_{ac}^c$ and c_1 is the combination of elastic moduli related to the averaged velocity of the sound wave [45,47].

For nonpolar optical scattering there is [48]

$$(\tau_{npo})^{-1}(k) = C_{npo}\left(E_{npo}^v\right)^2 F_{npo}, \quad (21)$$

$$C_{npo} = \frac{\pi kT\hbar}{\varrho(\hbar\omega_{op})^2 a_0^2}\frac{\partial k}{\partial\mathcal{E}}k^2, \quad (22)$$

in which $E_{npo}^v = E_{npo}^c$ are the nonpolar deformation potentials, $\hbar\omega_{op}$ is the energy of the optical phonon, ϱ is the crystal density, a_0 is the lattice constant.

Finally, the alloy disorder mechanism is described by [49,50]

$$(\tau_{ad})^{-1}(k) = C_{ad}(E_{ad}^v)^2 F_{ad}, \quad (23)$$

$$C_{ad} = \frac{4x(1-x)}{\pi\hbar\Omega}\frac{\partial k}{\partial\mathcal{E}}k^2, \quad (24)$$

where E_{ad}^v and E_{ad}^c are the matrix elements for the valence and conduction bands. The three modes above contain the common factor F_i,

$$F_i = [1 - L(1-y)]^2 - yH\frac{8}{3}, \quad (25)$$

where $y = E_i^v/E_i^c$.

For the parabolic band of heavy holes there is $H = 0$ in Eq. (17) and $F_i = 1$ in Eq. (25). According to the Wiedemann-Franz law [see Eq. (11)], the carrier thermal conductivity is proportional to the electrical conductivity. Since the latter is proportional to μ_H and for the HH band this mobility is quite low, the HH contribution to the thermal conductivity is negligible.

IV. RESULTS AND DISCUSSION

Our x-ray diffraction measurements revealed that the $Pb_{1-x}Cd_xTe$ samples grown by SSVG method maintain the rock-salt structure and high crystal quality with the single phase (see Figs. 4 and 2). The lattice parameter of $Pb_{1-x}Cd_xTe$ monocrystals decreases with x, following the Vegard's law with coefficient $da_0/dx = -0.43$ Å [26]. The value of this coefficient is higher than those obtained earlier by Rosenberg *et al.* [16] and Leute *et al.* [17] (−0.30 Å and −0.40 Å, respectively). That indicates that the number of Cd ions located in the interstitial positions in crystals grown by SSVG method is considerably lower than that obtained by other methods [13,19,25]. Results of low-temperature photoluminescence measurements in mid-infrared region shown in Fig. 1 indicate that substitution of Pb ions by Cd ones causes a linear increase of the fundamental energy gap with composition coefficient $dE_g/dx = 2.5$ eV in the investigated range of x. This increase is not as large as observed for elements like Mn or Eu in PbTe (dE_g/dx equal 4.8 and 5.8 eV, respectively) [51]. However, over twofold increase of L-point energy gap is observed for $x \approx 0.1$. This behavior is related to the considerably higher-energy gap of CdTe (1.6 eV at 4 K) compared to PbTe. Both effects, the decrease of the lattice parameter and the increase of the band gap of PbTe-CdTe mixed crystals, are in agreement with theoretical predictions based on density functional theory and tight-binding approach [6]. The energy gap of $Pb_{1-x}Cd_xTe$ increases almost linearly with

temperature: $dE_g/dT \approx$ 0.4–0.5 meV/K, which is similar to that observed for PbTe [52].

Our results report mostly transport properties of monocrystalline *p*-type $Pb_{1-x}Cd_xTe$ at room temperature with Cd content $0 \leqslant x \leqslant 0.102$. The first step in the theoretical description of the data is to separate contributions from the light- and heavy-hole valence bands. This is strictly related to the energy separation of the band edges and m^*_{hh} value. First, we take a tentative separation of these bands for PbTe and heavy holes' mass and tentatively divide the measured value of the total hole density into the LH and HH contributions. Next, we calculate the Fermi energies E_F^{lh} and E_F^{hh} using one of the formulas for LH band and its simplified version for the HH band with ΔE included. Then, by the iteration procedure we change the density distribution between the two bands and repeat the procedure until E_F^{lh} and E_F^{hh} become equal. This completes the distribution of holes between the two valence bands for a given value of x and the total hole density for assumed ΔE and value of m^*_{hh} [53,54]. Next, all the considered transport effects are calculated adjusting the other transport parameters until we reach overall optimal agreement between the experiment and theory. This procedure has the merit of keeping the theory close to the experimental reality. The specific band structure is illustrated in Fig. 7(a), which shows the band ordering of valence bands in PbTe and $Pb_{1-x}Cd_xTe$ near the L and Σ points of the Brillouin zone.

Electrical characterization revealed *p*-type conductivity of $Pb_{1-x}Cd_xTe$ for all cadmium contents with room-temperature hole densities varying between $(1.2–3.6) \times 10^{18}$ cm^{-3}. The hole density for $x = 0.02$ sample is about three times higher compared to pure PbTe. However, further increase of Cd content results in lowering the hole concentration from 3.6×10^{18} cm^{-3} to 1.8×10^{18} cm^{-3} for $x \approx 0.1$ as shown in Fig. 8(a). The determined experimental Hall mobility of $Pb_{1-x}Cd_xTe$ versus the Cd content x and its theoretical description for experimentally determined hole concentrations is shown in Fig. 8(b) (theoretical curves showing dependence of mobility on x for samples with constant hole concentrations 1×10^{18} cm^{-3} and 4×10^{18} cm^{-3} are presented in Fig. 9). It is seen that the mobility diminishes quite strongly with x. The main reason for the decrease is that, as seen in Fig. 7(b), when the Cd content grows, the HH band approaches in energy the LH band. In consequence, the contribution of HH to the total conduction increases and N_L decreases which is shown in Fig. 7(c). This lowers the total mobility [Eq. (13)] since the HH mobility is much lower than that of LH, due to their much heavier mass. The second reason for the fall of the mobility is that, as again seen in Fig. 7(b), the fundamental energy gap E_g between the L_6^- and L_6^+ bands grows with the content x. This results in the enhancement of the light-hole mass [see Eq. (5)], which further lowers the LH mobility in the L_6^+ band. Increasing role of HH with addition of Cd is also visible in our photoluminescence measurements. Smaller energy distance between the bands facilitates the diffusion of holes from L to Σ band reducing probability of radiative recombination of carriers. As a result, we observe more effective decay of photoluminescence with increasing temperature for samples with higher Cd content, as is shown in Fig. 5. Calculated contributions of individual scattering modes to the total hole mobility in $Pb_{1-x}Cd_xTe$ at $T = 300$ K versus Cd content x are shown in Fig. 10. Considering the results of our calculations, we can conclude that main scattering mechanisms at room temperature are the interaction with optical phonons and alloy disorder scattering. The second becomes dominant in the case of samples with $x \geqslant 0.03$. It is seen in Fig. 8(b) that our theoretical description of the measured mobility values is quite successful.

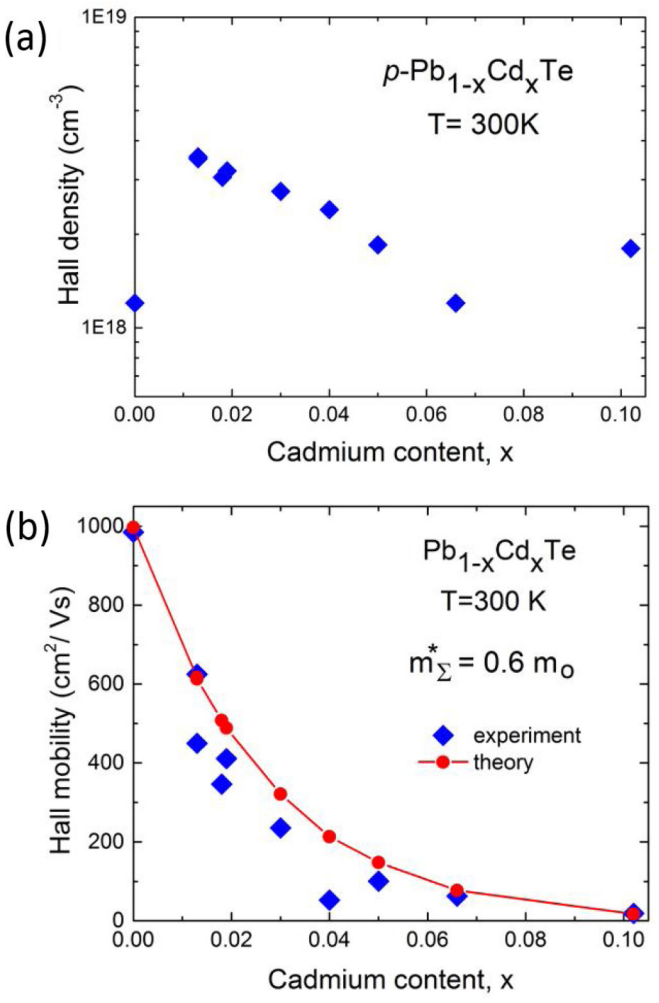

FIG. 8. Carrier density (a) and Hall mobility (b) in monocrystalline $Pb_{1-x}Cd_xTe$ alloy at room temperature averaged over light- and heavy-hole bands versus Cd content $0 \leqslant x \leqslant 0.102$. Full diamonds are experimental, circles are theoretical, the line is a guide to the eye.

Figure 11(a) shows experimental and theoretical results on the Seebeck coefficient α of $Pb_{1-x}Cd_xTe$ as a function of the Cd content. Similarly to Fig. 8, the experimental points are somewhat scattered since they correspond to different total hole densities determined experimentally. On the whole, α grows both experimentally and theoretically with increasing addition of Cd reaching 490 μV/K for highest x. However, observed enhancement [see Fig. 11(b)] is faster with respect to pure PbTe with decreasing hole concentration [so-called Pisarenko plot [55–57], solid line in Fig. 11(b)]. It is clearly seen in Fig. 11(c), where differences between measured values of the Seebeck coefficient and those expected for PbTe with appropriate hole densities are shown as a function of Cd

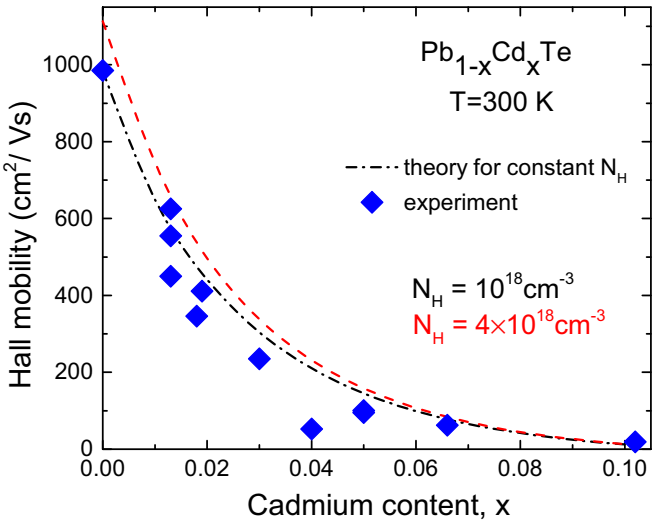

FIG. 9. Theoretical (dashed lines) dependence of mobility on x for $Pb_{1-x}Cd_xTe$ samples with single-hole concentration 1×10^{18} cm^{-3} and 4×10^{18} cm^{-3} compared to experimental data (diamonds) obtained for samples with different carrier concentration varying between $(1.2–3.6) \times 10^{18}$ cm^{-3}.

content x. It follows from the two-band formula (14) that the HH band contributes little to the total α because of the low HH mobility. It is difficult to judge the behavior of α from the exact but general expression (9), but it is possible to evaluate it more explicitly from an approximation applicable to partly degenerate carrier gas [38]. In the linear approximation in T one obtains $\alpha \sim Tm^*/N^{2/3}$, where m^* is the density of states effective mass at the Fermi level defined in Eq. (2). Then, it follows that the thermoelectric power grows with the increasing mass and diminishing LH density. This is roughly

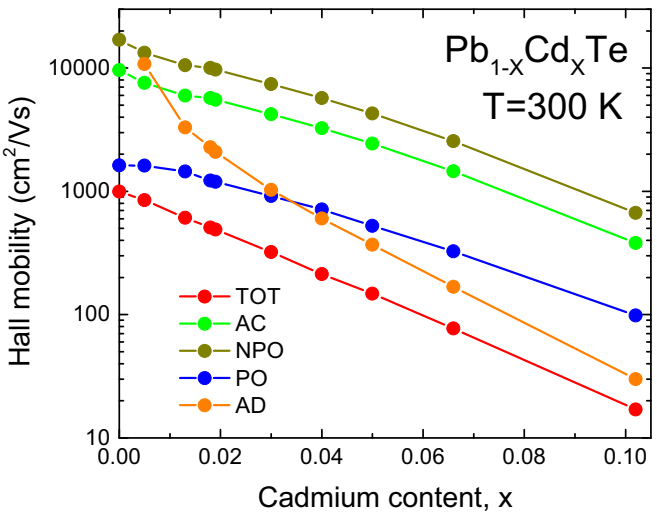

FIG. 10. Calculated contributions of individual scattering modes to the total hole mobility in $Pb_{1-x}Cd_xTe$ at $T = 300$ K versus Cd content x. TOT: total mobility, PO: polar optical interaction, AC: acoustic deformation potential, NPO: nonpolar optical interaction, AD: alloy disorder scattering. Calculations performed using the hole density obtained experimentally for given x [see Fig. 8(a)].

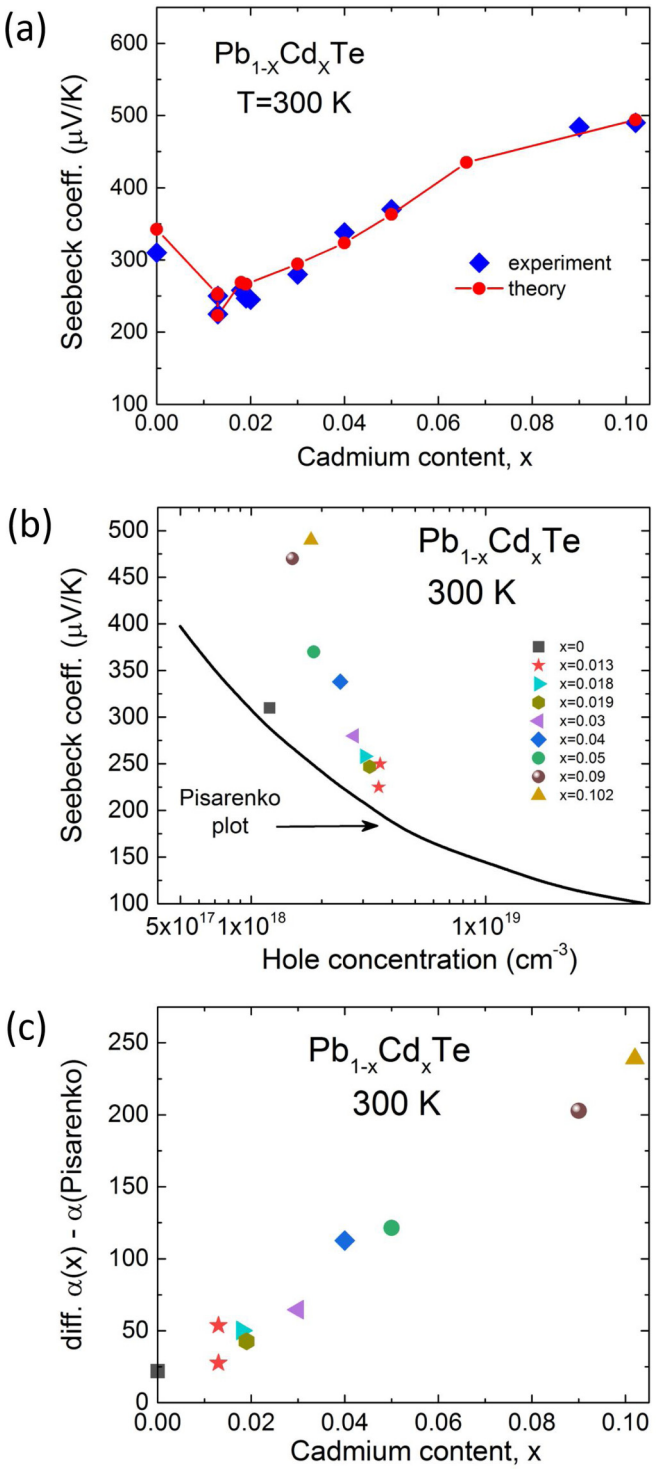

FIG. 11. The Seebeck coefficient of $Pb_{1-x}Cd_xTe$ at room temperature versus Cd content (a), carrier concentration (b). Gain of Seebeck coefficient related to the reference Pisarenko plot (c). Each experimental point is plotted for a sample with known x value and measured hole density [see Fig. 8(a)]. Line joins the theoretical points calculated for the corresponding parameters.

what one observes in Fig. 11. The calculation with the use of exact formula (9) gives the correct description of the data. In Fig. 12 we show the experimental and theoretical thermal conductivity κ of our $Pb_{1-x}Cd_xTe$ single crystals versus x. It

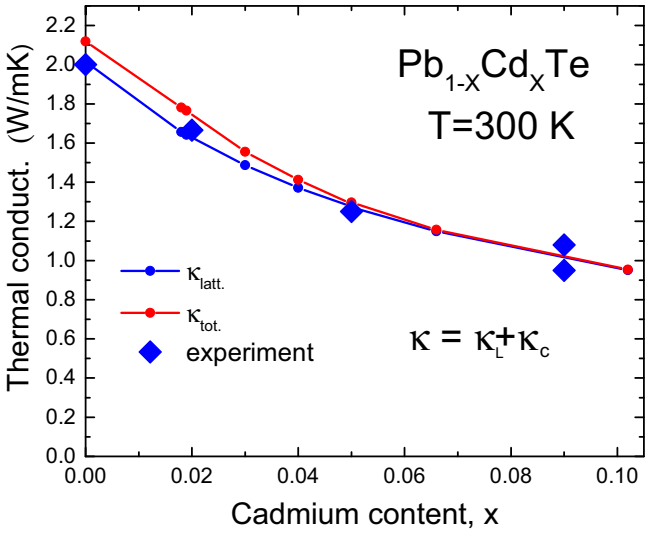

FIG. 12. Thermal conductivity of $Pb_{1-x}Cd_xTe$ versus Cd content. Squares are our experimental data, the lower line is theoretical for the lattice contribution to κ, the upper one takes additionally into account free holes contribution to total κ.

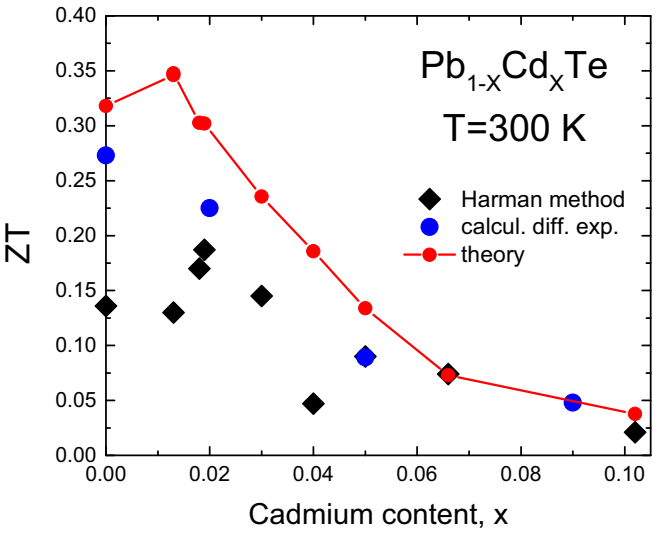

FIG. 13. Thermoelectric figure-of-merit parameter ZT of monocrystalline $Pb_{1-x}Cd_xTe$ at room temperature versus Cd content x as determined experimentally by two methods (see text). The theoretical line joins points calculated for given x and measured Hall carrier density.

is seen that addition of Cd decreases the total κ to 1 W/mK for samples with $x = 0.09$. The mobile hole contribution to the total κ is not large but not negligible, either. It follows from the formula (11) expressing the Wiedemann-Franz law that the low conductivity σ of HH band practically suppresses its contribution to κ. For this reason, the contribution of κ_c disappears at higher x. The dominating lattice part was calculated early using the theory of Callaway *et al.* and the more recent treatment of Tian *et al.* [42,43]. The general decrease of κ_L with growing x is due to the increasing alloy disorder scattering of acoustic phonons. The overall theoretical description of the data is very good.

Finally, Fig. 13 illustrates the measured and theoretical thermoelectric figure-of-merit parameter ZT of $Pb_{1-x}Cd_xTe$ versus Cd content x at $T = 300$ K. The data presented in Fig. 13 were obtained for samples with different hole concentrations [see Fig. 8(a)] resulting from slightly varying stoichiometry. Our experimental data are of two kinds. The full circles show values obtained by measuring separately σ, α, and κ and combining them into ZT according to the formula (12). On the other hand, the diamonds indicate results of ZT, as obtained directly by the Harman method. It can be seen that the Harman method gives consistently lower values of ZT. As in all figures above, the theoretical line is obtained by joining the points calculating the corresponding quantity for given values of x and the measured hole density N_H. Thus, the apparent theoretical maximum of ZT at $x = 1.3$ at.% is due to the high hole density 3.6×10^{18} cm^{-3} taken for the calculation. On the whole, the agreement between the theory and experiment should be considered as quite reasonable. It is seen that the overall increase of α cannot compensate the strong fall of the mobility shown in Fig. 8(b), thus, the ZT parameter decreases for higher Cd content. However, our calculations of ZT dependence on carrier concentration (see Fig. 14) performed for $x = 0.01$ sample suggest that, at $T = 300$ K, in this range of carrier density ZT parameter may change significantly. Optimal hole concentration maximizing ZT at room temperature should be $\approx 6 \times 10^{18}$ cm^{-3}. Moreover, extending our model for higher-hole densities and temperatures we found, as expected for PbTe-based thermolectrics, that ZT increases rapidly reaching $ZT \approx 1.4$ at $T = 600$ K for $N_h \approx 10^{20}$ cm^{-3}.

V. SUMMARY

We prepared the monocrystalline $Pb_{1-x}Cd_xTe$ samples up to $x \approx 0.1$ using SSVG method. Our monocrystals can serve as a reference for heavily doped, polycrystalline

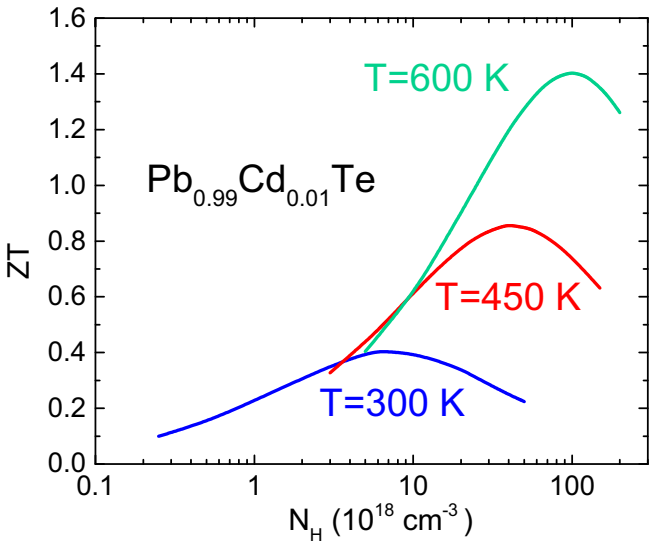

FIG. 14. Theoretical thermoelectric figure-of-merit parameter ZT of $Pb_{0.99}Cd_{0.01}Te$ versus carrier concentration at $T = 300$, 450, and 600 K.

PbTe-CdTe materials with Cd content limited to $x \approx 0.03$, which exhibit high thermoelectric figure of merit ($ZT = 1.2$–1.7) [13,14,25]. The optical L-point energy gap of $Pb_{1-x}Cd_xTe$ monocrystals determined from mid-infrared photoluminescence measurements grows with increasing Cd content and temperature, with $dE_g/dx = 2.5$ eV and $dE_g/dT \approx 0.4$–0.5 meV/K, respectively. Our results also indicate that alloying PbTe with Cd causes twofold enhancement of the Seebeck coefficient (up to $\approx$500 μV/K), which we attribute to the increased energy gap and growing contribution of Σ-band heavy holes. In parallel, we observe the reduction of thermal conductivity to 1 W/mK in $Pb_{1-x}Cd_xTe$ samples with highest x related to additional phonon scattering caused by substitutional Cd ions. As to the thermoelectric figure-of-merit parameter ZT, the benefit of more favorable thermopower and thermal conductivity is counteracted by a strong reduction of the hole mobility for samples with higher x, due to increased role of heavy holes. On the other hand, our theoretical analysis indicates very strong dependence of ZT on the hole concentration and temperature for samples with relatively small x. Thus, optimization of carrier density by additional doping or proper post-growth annealing may significantly improve ZT parameter of $Pb_{1-x}Cd_xTe$ monocrystals.

ACKNOWLEDGMENTS

The research was partially supported by the National Centre for Research and Development (Poland) through Grant TERMOD No. TECHMATSTRATEG2/408569/NCBR/2019 and by the Foundation for Polish Science through the IRA Programme co-financed by EU within SG OP.

APPENDIX

Below we list our parameters adjusted to fit all transport phenomena as well as formulas used to describe our photoluminesccence data shown in Fig. 5. For comparison, we also quote ΔE and m^*_{hh} values determined by other authors. Our listing does not pretend to be complete.

For PbTe at 300 K our values are $\Delta E = E(L_6^+) - E(\Sigma_{hh}) = 120$ meV; $m^*_{hh} = 0.6m_0$; deformation potentials $E^v_{ac} = E^c_{ac} = 12.75$ eV, $E^v_{npo} = E^c_{npo} = 16$ eV alloy disorder matrix elements: $E^v_{ad} = -2 \times 10^{-22}$ eV cm^{-3} and $E^c_{ad} = 10^{-22}$ eV cm^{-3}.

Other authors, $\Delta E = E(L_6^+) - E(\Sigma_{hh})$:
24 meV (Ref. [58])
40 meV (Ref. [59])
50 meV (Ref. [60])
60 meV (Ref. [61])
103 meV (Ref. [62,63])
120 meV (Ref. [64])
(100–150) meV (Ref. [41]).
m^*_{hh}:
$0.368m_0$ (Ref. [57])
$0.4m_0$ (Ref. [65])
$1m_0$ (Ref. [39])
$(0.6 - 2.5)m_0$ (Ref. [66]).

[1] G. J. Snyder and E. S. Toberer, Nat. Mater. **7**, 105 (2008).
[2] K. Dybko, M. Szot, A. Mycielski, A. Szczerbakow, P. Dziawa, M. Guziewicz, W. Knoff, E. Łusakowska, and T. Story, Appl. Phys. Lett. **108**, 133902 (2016).
[3] T. Schwarzl, M. Eibelhuber, W. Heiss, E. Kaufmann, G. Springholz, A. Winter, and H. Pascher, J. Appl. Phys. **101**, 093102 (2007).
[4] P. Dziawa, B. J. Kowalski, K. Dybko, R. Buczko, A. Szczerbakow, M. Szot, E. Łusakowska, T. Balasubramanian, B. M. Wojek, M. H. Berntsen, O. Tjernberg, and T. Story, Nat. Mater. **11**, 1023 (2012).
[5] K. Dybko, M. Szot, A. Szczerbakow, M. U. Gutowska, T. Zajarniuk, J. Z. Domagała, A. Szewczyk, T. Story, and W. Zawadzki, Phys. Rev. B **96**, 205129 (2017).
[6] M. Bukała, P. Sankowski, R. Buczko, and P. Kacman, Phys. Rev. B **86**, 085205 (2012).
[7] Y. Pei, H. Wang, Z. M. Gibbs, A. D. LaLonde, and G. J. Snyder, NPG Asia Mater. **4**, e28 (2012).
[8] L. M. Rogers and A. J. Crocker, J. Phys. D: Appl. Phys. **5**, 1671 (1972).
[9] A. J. Crocker and B. J. Sealy, J. Phys. Chem. Solids **33**, 2183 (1972).
[10] Y. Pei, H. Wang, and J. Snyder, Adv. Energy Mater. **24**, 6125 (2012).
[11] Y. Xiao and L. D. Zhao, npj Quantum Mater **3**, 55 (2018).
[12] E. Smajek, M. Szot, L. Kowalczyk, V. Domukhovski, B. Taliashvili, P. Dziawa, W. Knoff, E. Łusakowska, A. Reszka, B. J. Kowalski, M. Wiater, T. Wojtowicz, and T. Story, J. Cryst. Growth **323**, 140 (2011).
[13] K. Ahn, M. K. Han, J. He, J. Androulakis, S. Ballikaya, C. Uher, V. P. Dravid, and M. G. Kanatzidis, J. Am. Chem. Soc. **132**, 5227 (2010).
[14] G. Tan, X. Zhang, S. Hao, H. Chi, T. P. Bailey, X. Su, C. Uher, V. P. Dravid, Ch. Wolverton, and M. G. Kanatzidis, ACS Appl. Mater. Interfaces **11**, 9197 (2019).
[15] J. P. Heremans, V. Jovovic, E. S. Toberer, A. Sarmat, K. Kurosaki, A. Charoenphakdee, S. Ymanaka, and G. J. Snyder, Science **321**, 554 (2008).
[16] A. J. Rosenberg, R. Grierson, J. C. Woolley, and P. Nikolic, Trans. Metal. Soc. AIME **230**, 342 (1964).
[17] R. Leute and V. Schmidt, Z. Phys. Chem. **172**, 81 (1991).
[18] P. M. Nikolic, Br. J. Appl. Phys. **17**, 341 (1966).
[19] T. Scheidt, E. G. Rohwer, H. M. Von Bergmann, E. Saucedo, E. Diéguez, L. Fornaro, and H. Stafast, J. Appl. Phys. **97**, 103104 (2005).
[20] M. Szot, K. Dybko, P. Dziawa, L. Kowalczyk, E. Smajek, V. Domukhovski, B. Taliashvili, P. Dłużewski, A. Reszka, B. J. Kowalski, M. Wiater, T. Wojtowicz, and T. Story, Cryst. Growth Des. **11**, 4794 (2011).
[21] M. Szot, K. Dybko, P. Dziawa, L. Kowalczyk, V. Domukhovski, B. Taliashvili, A. Reszka, B. Kowalski, P. P. Dłużewski, M. Wiater, T. Wojtowicz, and T. Story, Funct. Mater. Lett. **7**, 1440007 (2014).

[22] W. Heiss, H. Groiss, E. Kaufmann, G. Hesser, M. Böberl, G. Springholz, F. Schäffler, K. Koike, H. Harada, and M. Yano, Appl. Phys. Lett. **88**, 192109 (2006).

[23] H. Groiss, E. Kaufmann, G. Springholz, T. Schwarzl, G. Hesser, F. Schäffler, W. Heiss, K. Koike, T. Itakura, T. Hotei, M. Yano, and T. Wojtowicz, Appl. Phys. Lett. **91**, 222106 (2007).

[24] K. Koike, H. Harada, T. Itakura, M. Yano, W. Heiss, H. Groiss, E. Kaufmann, G. Hesser, and F. Schäffler, J. Cryst. Growth **301-302**, 722 (2007).

[25] Y. Pei, A. D. LaLonde, N. A. Heinz, and G. J. Snyder, Adv. Energy Mater. **2**, 670 (2012).

[26] M. Szot, A. Szczerbakow, K. Dybko, L. Kowalczyk, E. Smajek, V. Domukhovski, E. Łusakowska, P. Dziawa, A. Mycielski, T. Story, M. Bukała, M. Galicka, P. Sankowski, R. Buczko, and P. Kacman, Acta Phys. Pol. A **116**, 959 (2009).

[27] A. Szczerbakow and K. Durose, Prog. Cryst. Growth Charact. Mater. **51**, 81 (2005).

[28] A. Szczerbakow and H. Berger, J. Cryst. Growth **139**, 172 (1994).

[29] A. J. Crocker and L. M. Rogers, J. Phys. Coll. **29**, 129 (1968).

[30] K. Dybko, P. Pfeffer, M. Szot, A. Szczerbakow, A. Reszka, T. Story, and W. Zawadzki, New. J. Phys. **18**, 013047 (2016).

[31] Z. Gołacki, M. Górska, T. Warminski, and A. Szczerbakow, J. Cryst. Growth. **74**, 129 (1986).

[32] B. A. Orłowski, A. Szczerbakow, B. J. Kowalski, M. A. Pietrzyk, K. Gas, M. Szot, W. Szuszkiewicz, V. Domukhovski, A. Reszka, S. Mickevicius, R. L. Johnson, S. Thiess, and W. Drube, J. Electron. Spectrosc. Relat. Phenom. **184**, 199 (2011).

[33] N. Berchenko, T. Story, M. Trzyna, S. Fadeev, K. Kurbanov, S. Adamiak, W. Bochnowski, A. Dziedzic, and J. Cebulski, Surf. Interface Anal. **48**, 547 (2016).

[34] T. C. Harman, J. Appl. Phys. **29**, 1373 (1958).

[35] T. C. Harman, J. H. Cahn, and M. J. Logan, J. Appl. Phys. **30**, 1351 (1959).

[36] Ch. M. Jaworski, M. D. Nielsen, Hsin Wang, S. N. Girard, Wei Cai, W. D. Porter, M. G. Kanatzidis, and J. P. Heremans, Phys. Rev. B **87**, 045203 (2013).

[37] J. O. Dimmock, in *Physics of Semimetals and Narrow Gap Semiconductors*, edited by D. L. Carter and R. T. Bate (Pergamon, Oxford, 1971), p. 363.

[38] W. Zawadzki, Adv. Phys. **23**, 435 (1974).

[39] G. Nimtz and B. Schlicht, in *Narrow-Gap Semiconductors* edited by G. Hoehler, Springer Tracts in Modern Physics Vol. 98 (Springer, Berlin, 1983).

[40] J. N. Zemel, J. D. Jensen, and R. B. Schoolar, Phys. Rev. **140**, A330 (1965).

[41] Z. M. Gibbs, H. Kim, H. Wang, R. L. White, F. Drymiotis, M. Kaviany, and G. J. Snyder, Appl. Phys. Lett. **103**, 262109 (2013).

[42] Z. Tian, J. Garg, K. Esfarjani, T. Shiga, J. Shiomi, and G. Chen, Phys. Rev. B **85**, 184303 (2012).

[43] J. Callaway and H. von Baeyer, Phys. Rev. **120**, 1149 (1960).

[44] E. H. Putley, J. Phys. C: Solid State **8**, 1837 (1975).

[45] Y. I. Ravich, B. A. Efimova, and V. I. Tamarchenko, Phys. Status Solidi **43**, 453 (1971).

[46] P. Pfeffer and W. Zawadzki, Phys. Status Solidi (b) **88**, 247 (1978).

[47] C. Herring and E. Fogt, Phys. Rev. **101**, 944 (1956).

[48] D. M. Zayachuk, Fiz. Tekh. Poluprovodn. **31**, 281 (1997) [Semiconductors **31**, 173 (1997)].

[49] J. Kossut, Phys. Status Solidi B **86**, 593 (1978).

[50] K. Takita, T. D. Thanh, and S. Tanaka, Phys. Stats Solidi B **149**, 80 (1977).

[51] T. Story, in *Lead Chalcogenides: Physics and Applications*, edited by D. Khokhlov (Taylor and Francis, New York, 2003), p. 394.

[52] K. Koike, T. Honden, I. Makabe, F. P. Yan, and M. Yano, J. Cryst. Growth **257**, 212 (2003).

[53] G. Karczewski, L. Świerkowski, T. Story, A. Szczerbakow, J. Niewodniczanska-Blinowska, and G. Bauer, Semicond. Sci. Technol. **5**, 1115 (1990).

[54] T. Story, G. Karczewski, L. Świerkowski, and R. R. Gałązka, Phys. Rev. B **42**, 10477 (1990).

[55] A. F. Ioffe, *Physics of Semiconductors* (Academic, New York, 1960).

[56] J. P. Heremans, B. Wiendlocha, and A. M. Chamoire, Energy Environ. Sci. **5**, 5510 (2012).

[57] C. J. Vineis, T. C. Harman, S. D. Calawa, M. P. Walsh, R. E. Reeder, R. Singh, and A. Shakouri, Phys. Rev. B **77**, 235202 (2008).

[58] Y. Gelbstein, Z. Dashevsky, and M. Dariel, J. Appl. Phys. **104**, 033702 (2008).

[59] Y. I. Ravich, Lead chalcogenides, in *Physics and Applications*, edited by D. Khokhlov (Taylor and Francis, New York, 2003), p. 3.

[60] H. Sitter, K. Lischka, and H. Heinrich, Phys. Rev. B **16**, 680 (1977).

[61] Y. Pei, X. Shi, A. Lalonde, H. Wang, L. Chen, and G. J. Snyder, Nature (London) **473**, 66 (2011).

[62] R. S. Allgaier and B. B. Houston, J. Appl. Phys. **37**, 302 (1966).

[63] J. Zhao, C. D. Malliakas, K. Wijayaratne, V. Karlapti, N. Appathurai, D. Y. Chung, S. Rosenkranz, M. G. Kanatzidis, and U. Chatterjee, Europhys. Lett. **117**, 27006 (2017).

[64] S. V. Airapetyants, M. N. Vinogradova, I. N. Dubrovskaya, N. V. Kolomoets, and I. M. Rudnik, Fiz. Tverd. Tela **8**, 1336 (1966) [Sov. Phys.–Solid State **8**, 1069 (1966)].

[65] L. M. Rogers and A. J. Crocker, J. Phys. D: Appl. Phys. **4**, 1006 (1971).

[66] *Landolt-Bornstein: Numerical Data and Functional Relationship in Science and Technology–New Series*, edited by O. Madelung (Springer, Berlin, 1983), Vol. 17.